

## A Permanent Magnet Synchronous Motor for Traction Applications of Electric Vehicles

Smrutiranjannayak, Shagufta Shahnaz, Debendra Kumar Sahoo, Smitasree Jena

Department of Electrical Engineering, NM Institute of Engineering and Technology, Bhubaneswar, Odisha

Department of Electrical Engineering, Raajdhani Engineering College, Bhubaneswar, Odisha

Department of Electrical Engineering, Aryan Institute of Engineering and Technology Bhubaneswar, Odisha

Department of Electrical Engineering, Capital Engineering College, Bhubaneswar, Odisha

**ABSTRACT-** This paper presents the design of a Permanent Magnet Synchronous Motor (PMSM) for traction applications of electric vehicles (EVs). The design is based on the stator geometry of an existing commercial available induction traction motor. The rotor configurations considered in this study are the surface mounted magnet (SPM) and the inset permanent magnet (IPM) types. Both designs are investigated for the identical specification and their overall performances are compared with the existing asynchronous motors. A schematic block diagram of the design flow chart applied is illustrated. An analytical approach for calculating stator iron loss [1] is applied in the design procedure to ensure the required performance is reached. A thermal analysis of the prototype motor based on the lumped-circuit model and finite element analysis is also presented. Lastly, conclusions on the overall performance of PMSMs for electric vehicle applications are made and discussed.

### I. INTRODUCTION

With the worldwide trend to energy conservation, there is a need to increase the efficiency of electrical machine drives, particularly a.c. drives. The recent advancements of permanent magnet (PM) materials, solid-state devices and microelectronics have contributed to new energy efficient, high performance electric drives that use modern PM brushless or synchronous motors. Owing to rare-earth PMs, these motors present higher efficiency, power factor, power density and better dynamic performance than asynchronous motors without sacrificing reliability [2]. It has also been shown that these motors can be operated over a wide constant power speed range [3]. Not surprisingly, a vast amount of attention has been given to these motors in a variety of automotive applications, e.g. traction applications of electric vehicles.

This paper deals with the design and verification of PMSMs for the electric vehicle propulsion applications. The design study is based on the stator geometry of an existing asynchronous truck motor. Two rotor types studied in the design are the surface mounted PM (SPM) and inset PM (IPM) configurations, as depicted in Fig. 1. In order to achieve the required overall performance of the drive, various operating loss estimations are embedded into the design procedure. The predictions of these losses, especially iron

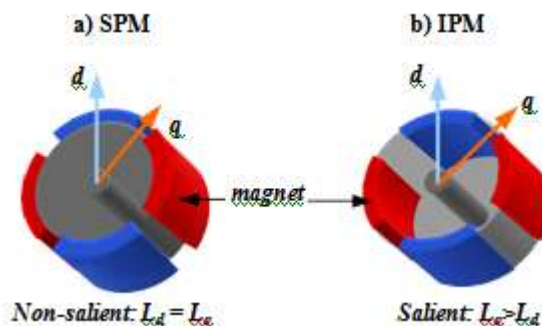


Fig. 1. Rotor configurations studied: a) Surface Mounted PM (SPM);

b) Inset PM (IPM)

losses, are particular indispensable for drives with a deep- field weakening range. The analytical approach applied to predict iron losses in the design procedures is based on the proposed models in [1]. Two thermal design packages, Motor-CAD [4] and FEMLAB [5], are also used in gaining insight of where the thermal design can be compromised and foreseeing the thermal “hot-spot” within the design. The expected performances of the PMSM prototype motor are compared with the existing induction motor drive.

## II. DESIGN SPECIFICATIONS

### A. Stator Geometry

The PMSM designs in this study are based on the existing induction motor stator geometry, the stator outside diameter is 188mm and the machine active length is 165 mm. The induction motor stator geometry can be referred to Fig. A1 in Appendix.A.

### B. Performance Characteristics Required

The performance characteristics of the induction motor drive are shown in Fig. 2. The desired performance of the PMSM prototype is expected to at least meet the rated electromagnetic torque and power specifications. Particular attentions are focused when the motor is operating above the rated speed in constant power or field-weakening region.

### Performance Characteristics of the asynchronous motor drive

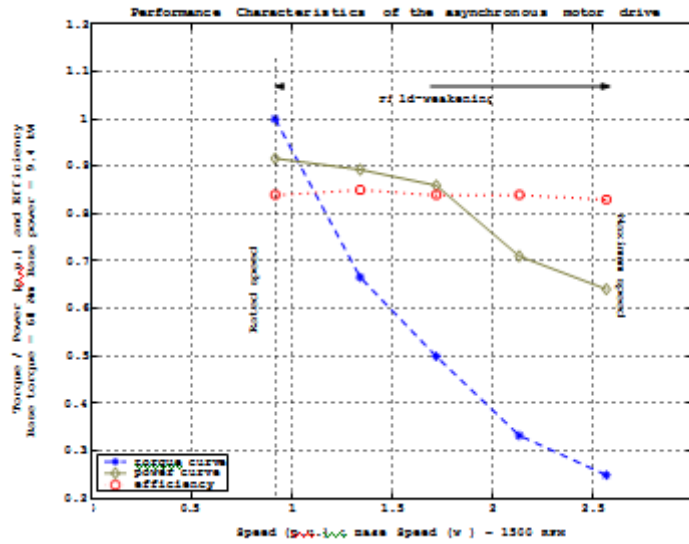


Fig. 2. Performance characteristics of the induction motor drive.

Constant Power Speed Range (CPSR) with a figure of 2.57 is necessary and CPSR is defined as the ratio of the maximum operating speed over the rated speed of the motor. This implies that a maximum operating speed of about 3900RPM is required. The proposed intermittent drive cycle is described as illustrated in Fig.3.

## III. THEORY

### A. Torque and EMF of PMSMs

The electromagnetic torque developed by a PMSM can be expressed as a function of the angle  $(\theta + \gamma)$  between the d-axis (excitation magnetic flux  $\Phi_{axis}$ ) and the armature current  $I_a$ , as shown in (1).

$$T_d = k_T \Phi_f I_a \sin(\theta + \gamma) \quad (1)$$

where  $k_T$  is the torque constant. For  $N_1 k_w$  turns, where  $k_w$  is the winding factor, the rms EMF is

$$E_f \approx E_{f1} = \frac{2\pi}{\sqrt{2}} \left( \frac{\pi}{4} - N_1 \right) k_{f1} f \Phi_1 = k_f \omega \Phi_1 \quad (2)$$

where  $k_f$  is the EMF constant.

where  $k_f$  is the EMF constant.

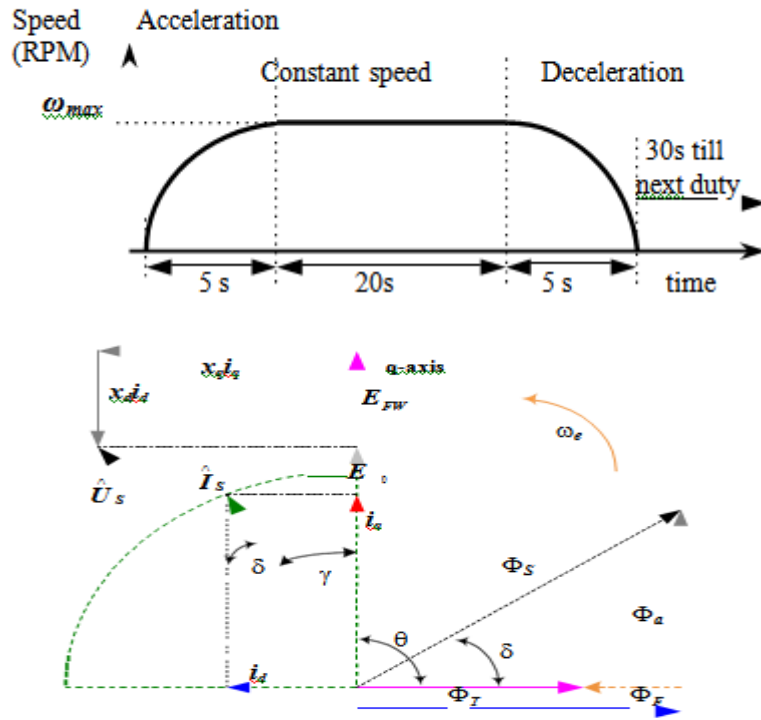


Fig. 4. Phasor diagram of PMSMs in d-q axis representation.

B. Field-weakening and Motor Model

Fig. 4 shows a phasor diagram of a salient PMSM in d-and q-axes representation. A “fixed excitation flux “ from magnets is constantly present in PMSMs, flux control or field- weakening is achieved by introducing an imposing field against this fixed excitation field. The magnitude of the imposing field is directly controlled by the current angle  $\gamma$  and d-axis current  $I_d$  increases or decreases as  $\gamma$  varies. When operating at rated voltage above the rated speed, the voltage can be expressed as

$$V_R^2 \geq \omega^2 \left[ (\Phi_M + l_d i_d)^2 + (l_q i_q)^2 \right] \quad (3)$$

where  $\omega$  is the electrical speed in radians per second.

A schematic diagram of an inverter fed PMSM is depicted in Fig. 5. The basic voltage current relations can be described as

$$\begin{bmatrix} |V_{an}| \\ |V_{bn}| \\ |V_{cn}| \end{bmatrix} = \begin{bmatrix} R_s & 0 & 0 \\ 0 & R & 0 \\ 0 & 0 & R_s \end{bmatrix} \begin{bmatrix} |i_a| \\ |i_b| \\ |i_c| \end{bmatrix} + \begin{bmatrix} L & M & M \\ M & r & M \\ M & M & L \end{bmatrix} \begin{bmatrix} |i_a| \\ |i_b| \\ |i_c| \end{bmatrix} + \begin{bmatrix} e_a \\ e_b \\ e_c \end{bmatrix} \quad (4)$$

where  $R_s$  winding resistance perphase  
 $L$  self inductance perphase  
 $M$  mutual inductance between phases  
 $e$  per phase EMF  
 $V$  per phase voltage  
 $\xi$  Laplace operator

In the study, a dc voltage  $V_{dc}$  source of 48 volts is assumed and the fundamental line-to-line rms voltage  $V_{L-L(RMS)}$  is

$$V_{L-L(RMS)} = \frac{\sqrt{3}}{\pi} V_{DC} \quad (5)$$

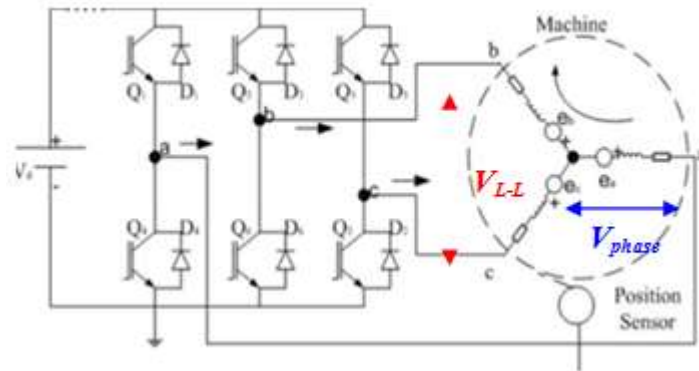


Fig. 5. Inverter fed PMSMs.

when the inverter is operating in a square-wave mode. The peak phase voltage  $V_{phase}$  available is then

$$\hat{V}_{phase} = V_{L-L(RMS)} \cdot \sqrt{\frac{2}{3}} \quad (6)$$

#### IV. ELECTROMAGNETIC DESIGN

##### A. Parameter Study

As aforementioned, the possibility of using an existing induction motor stator geometry is explored in this study. Subsequently, the winding configuration of the PMSM prototype is identical to the one used in induction motor (IM). With this respect of the study, focus has been only placed on the three geometric parameters:

- Size of the air gap,  $\delta$ .
- Thickness of the magnet,  $l_m$ .
- Magnet span / coverage,  $2\alpha$ .

The influences of these parameters on the torque-speed performance characteristic are illustrated in Fig. 6. The comparison in performance between SPM and IPM is presented in Fig. 9. It can be noted that IPM design has a higher rated torque. This is due to the additional reluctance torque generated from the rotor saliency.

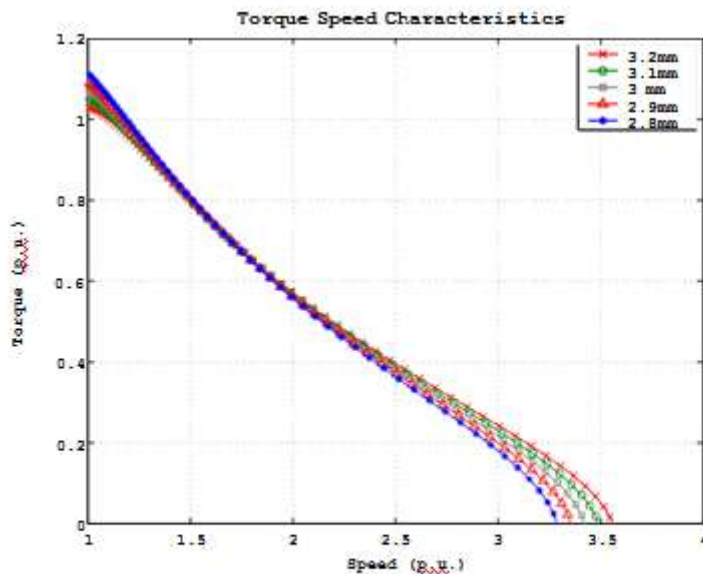


Fig. 6. Torque-speed characteristics in the field-weakening region ( $l_m=2\text{mm}$ ,  $2\alpha=120^\circ\text{elec.}$  and  $\delta$  is varying).

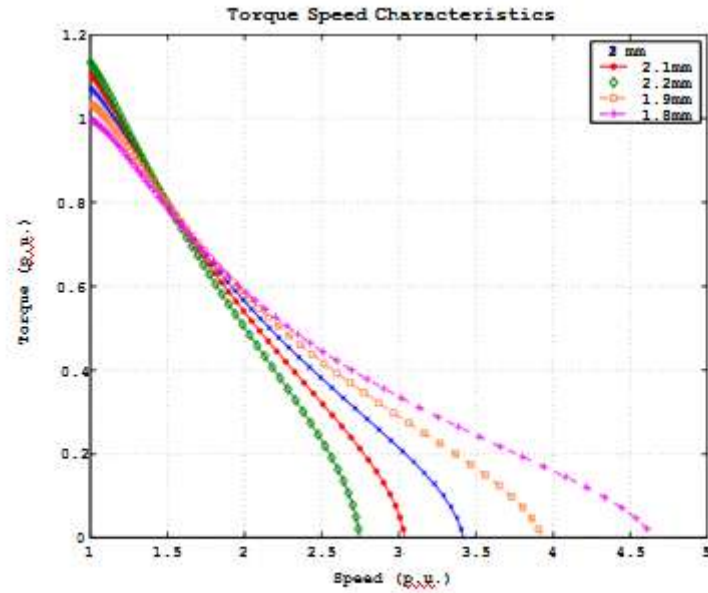


Fig. 7. Torque-speed characteristics in the field-weakening region ( $\delta=3\text{mm}$ ,  $2\alpha=120^\circ\text{elec.}$  and  $l_m$  is varying).

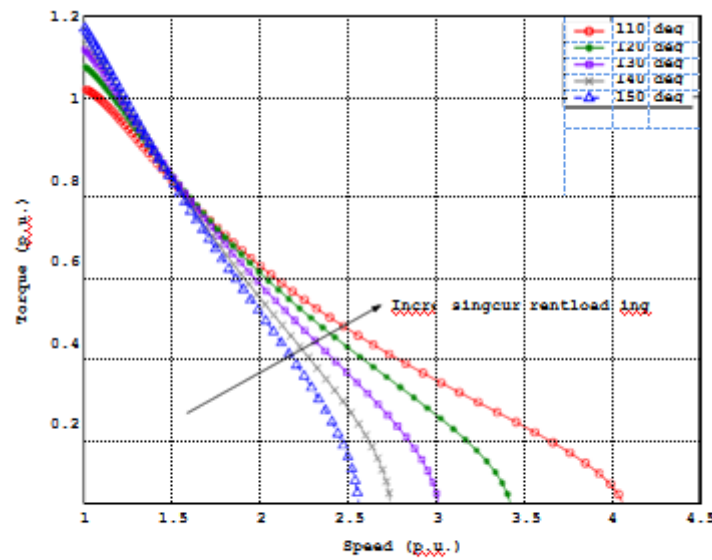


Fig. 8. Torque-speed characteristics in the field-weakening region ( $l_m=2\text{mm}$ ,  $\delta=3\text{mm}$  and magnet span  $2\alpha$  is varying).

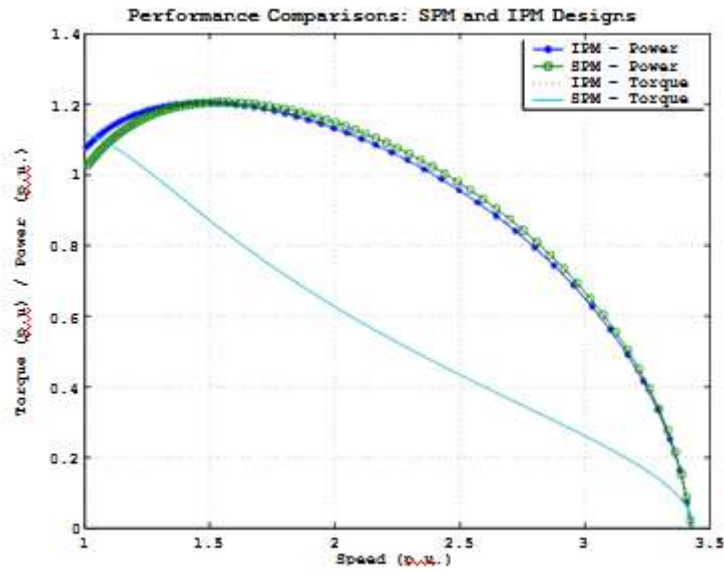


Fig. 9. Performance curves of IPM and SPM.

#### B. Magnet Protection

When the motor is operated at maximum load condition, the linear current density in the stator must be constrained so that no demagnetization of the magnet occurs. According to Slemon[6], the criterion for magnet protection from the demagnetisation by the armature reaction can be derived from the flux density waveform in the air gap investigation. The thermal model of Motor-CAD is based on the lumped-circuit analysis, and FEMLAB is based on the finite element analysis (FEA). The motor is natural cooled as in the case of the existing induction motor drive. Fig. 10 shows the duty cycle used in Motor-CAD for the analysis. The temperature rise in various parts of the motor after 10 minutes operation is presented in Fig.11.

$$\hat{B}_s = \frac{l_m}{g_s} \quad (7)$$

where

$$\hat{B}_s = \frac{2\sqrt{2} \cdot r \cdot \mu_0 \cdot S_{1S}}{p \cdot g_s} \quad (8)$$

as the maximum value of the sinusoidally distributed air gap flux density from the stator current. Hence, the linear current density (in RMS value) constraint is given by

$$S_{1S} \leq \frac{p g_s}{2\sqrt{2} \cdot r \mu_0 \sin \alpha} \cdot k \cdot \left( \frac{l_m}{g_s} B_r - B_d \right) \cdot \text{safety} \quad (9)$$

where  $\text{safety}$  is introduced as safety margin.

### C. Number of Turns per slot

As mentioned previously in section III, and shown in Fig.4, the magnitude of the voltage phasor above the rated speed can be expressed as (3). Hence, the number of turns per slot  $n_s$  can be calculated as

$$n_s^2 = \frac{V^2}{\left[ \left( k_{a1} q B_r D_{in} L \omega - c_1 n_s I \cdot \sin \gamma_b \right)^2 + \left( c n_2 I \cdot \cos \gamma_b \right)^2 \right]} \quad (10)$$

where

$$c_1 = \frac{6 \cdot (q n_s)^2 r L}{\mu_0 g_s \left( \frac{l}{g_s} + \frac{m}{\mu_r} \right)} \quad (11)$$

$$c_2 = \frac{6 \cdot (q n_s)^2 r L}{\mu_0 \cdot g_s} \quad \dots$$

$$n_s I = \frac{4T}{D_{in} L B_r Q_s} \quad (13)$$

## V. THERMAL ANALYSIS

In this section, the thermal analysis used in the design process is described. Two commercially available thermal design packages, Motor-CAD and FEMLAB, are used in our

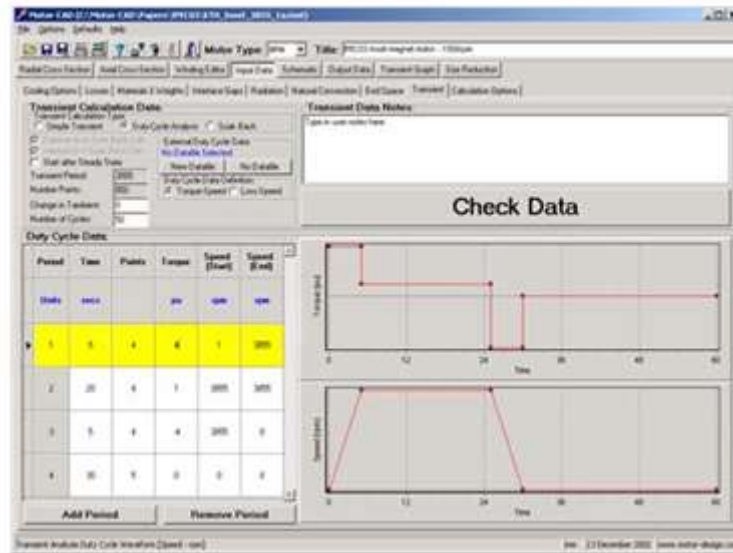


Fig. 10. Motor-CAD duty cycle editor.

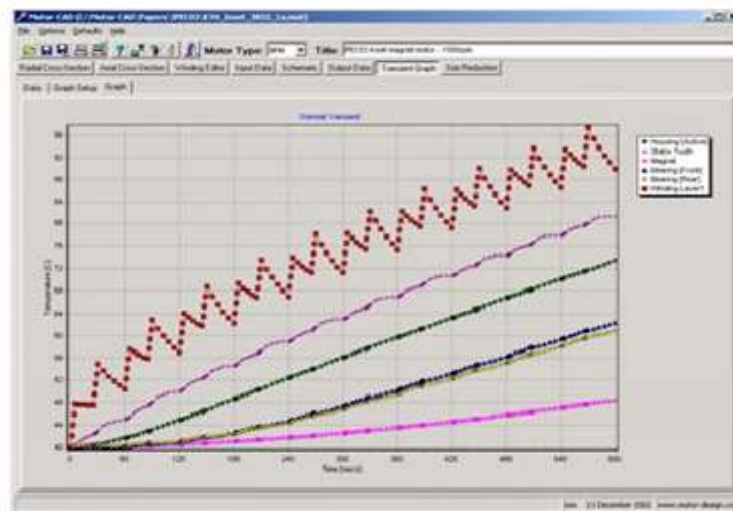


Fig. 11. Temperature rise after 10 minutes.

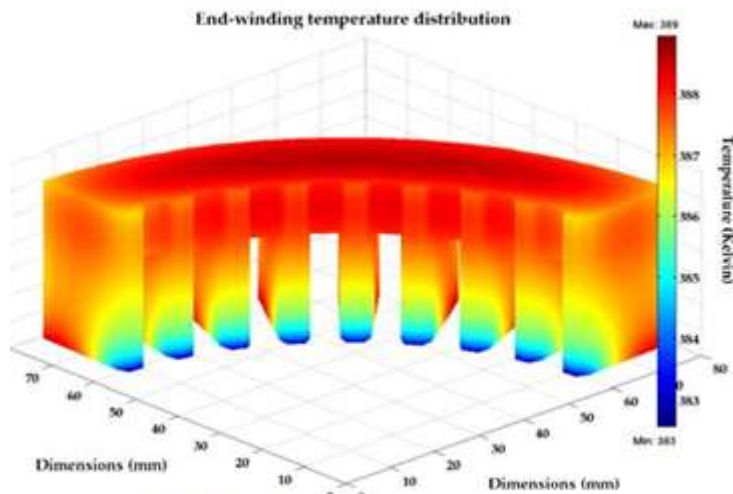


Fig. 11. 3D-FEMLAB: End-winding temperature distribution.

Fig. 11 illustrates the end-winding temperature distribution from a 3D FEMLAB simulation. Strengths and weaknesses of the two approaches can be found in[7].

### VI. DESIGNPROCEDURES

A schematic of the design flow chart applied in this study is depicted in Fig. 12. With the given drive specifications and the stator geometry, parametric studies on motor performances are carried out for both SPM and IPM designs, as described in section IV. Demagnetization check with a certain safety margin is used to ensure the absolute magnet protection.

### VII. PROTOTYPE

In this section, the details of an IPM prototype motor built are presented. Fig. 13 shows the various parts of the motor. The back EMF at no load condition at rated speed of 1500 rpm is depicted in Fig. 14.

#### A. Measurements

Cogging torque is measured and compared with the results from the FEM simulations, as shown in Fig. 15. The measured no load iron loss is compared with the FEM results and analytical predictions. As shown in Fig. 16, analytical predictions represent a good trend or best-fit curve of the measurement values. However, larger discrepancies up to 20% are noted. This is expected due to the errors in the measurement setup and assumptions made in calculating the windage and friction losses.

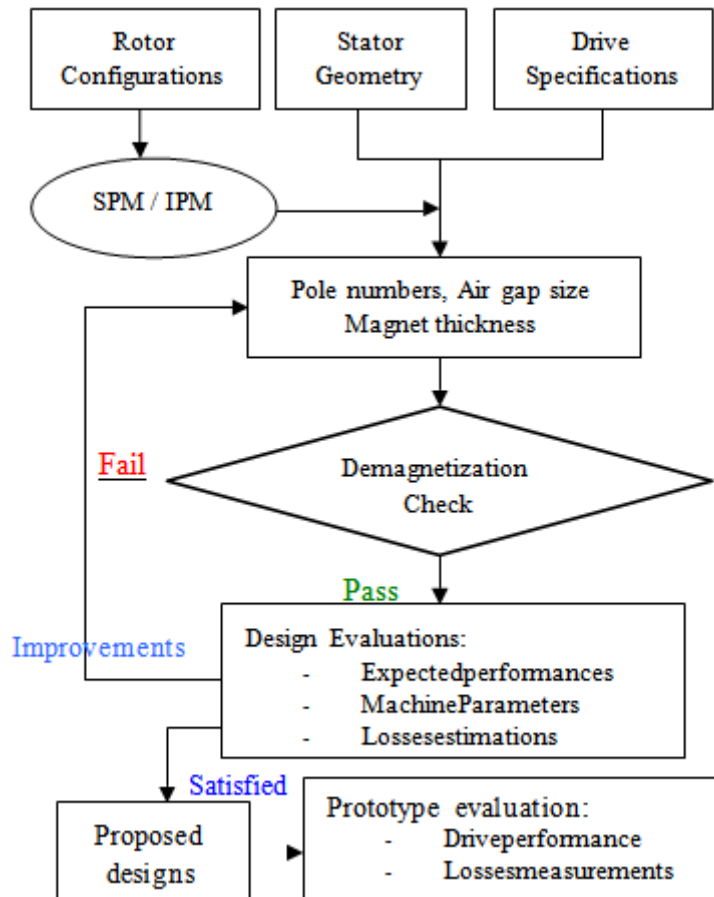


**Fig. 12.** The schematic of the design flow chart.



Fig. 13. Testing bench.

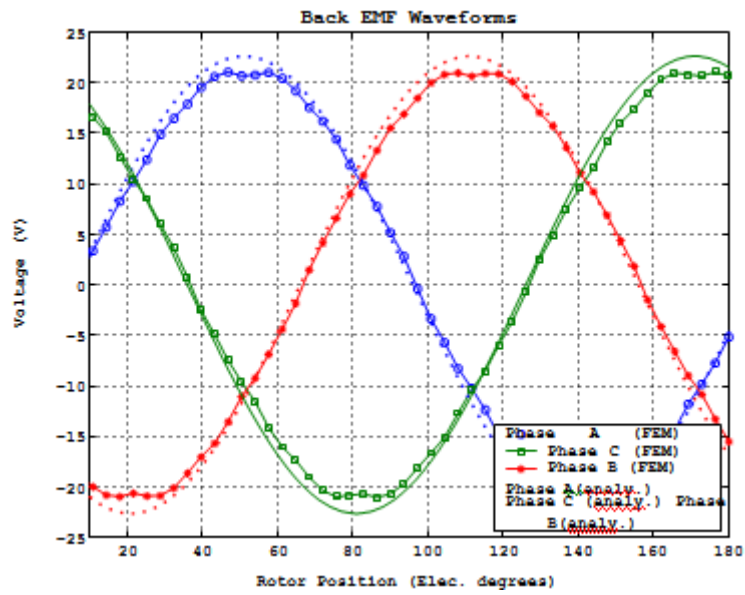


Fig. 14. Back EMF at 1500RPM.

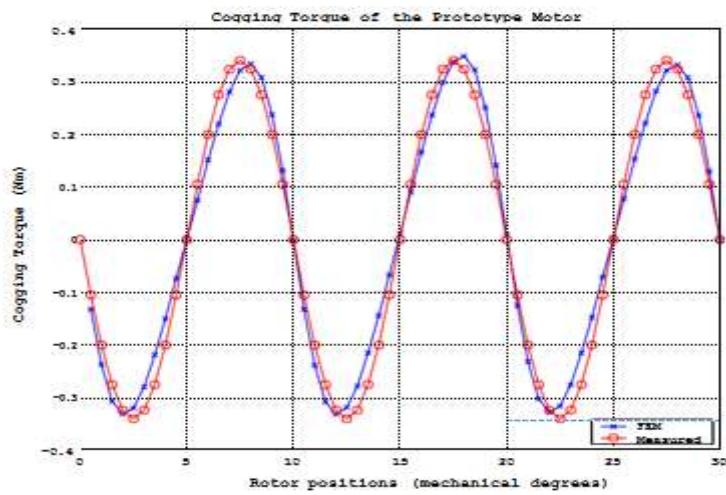


Fig. 15. Cogging torque of the prototype motor.

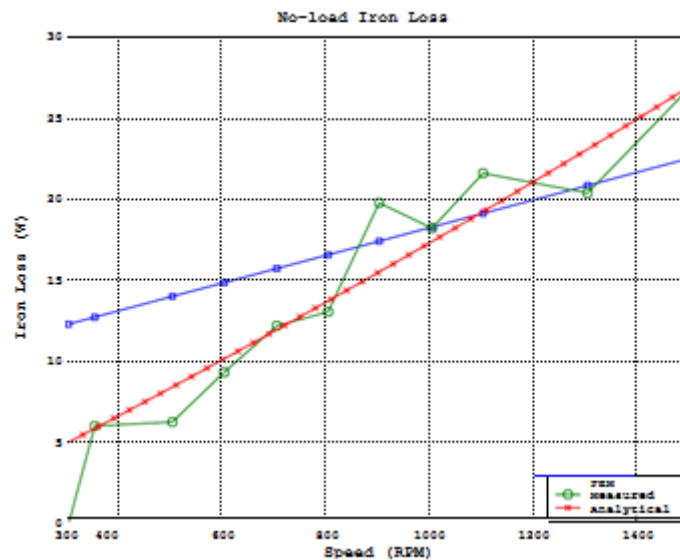


Fig. 16. No-load iron loss.

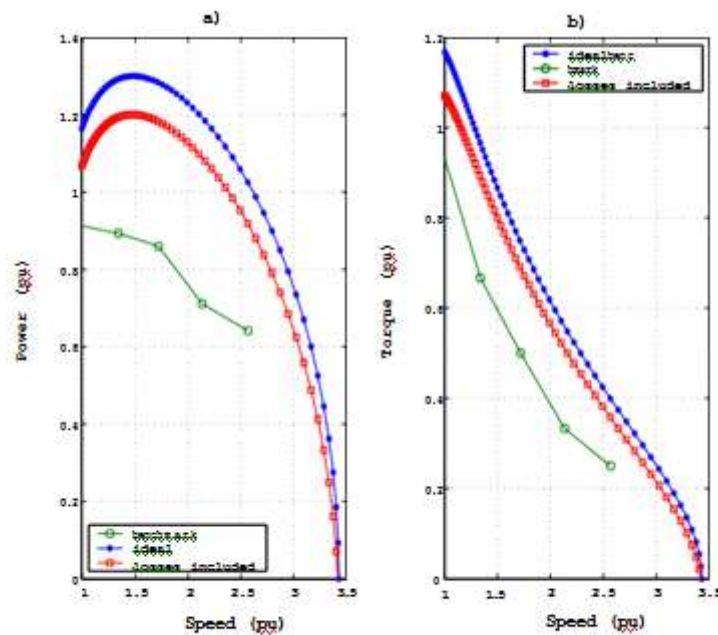


Fig. 17. Expected performance of the prototype motor.

LIST OF PRINCIPAL SYMBOLS

- $k_{w1}$  fundamental stator winding factor
- $g_e$  equivalent airgap
- $q$  number of slots per pole per phase  $D_{in}$  stator inner diameter / bore diameter  $L$  active length
- $B_\delta$  peak air gap flux density
- $S$  linear current loading
- $l_m$  magnet thickness
- $N_1$  number of turns per phase
- $k_f$  stator fill factor
- $E_{f1}$  fundamental back EMF
- $\square_m$  magnet flux
- $\square_1$  fundamental flux per pole
- $L_d$  d-axis inductance
- $L_q$  q-axis inductance
- $i_d$  d-axis current

- $i_q$  q-axis current
- $V_R$  rated voltage
- $\omega$  angular frequency in radians per second
- $B_r$  remanent flux density
- $B_d$  demagnetization flux density
- $Q_s$  number of stator slots
- $p$  pole numbers
- $\mu_0$  air permeability
- $\mu_r$  relative permeability
- $D_{in}$  stator bore diameter

TABLE A1 DIMENSIONS OF THE STATOR

| PARAMETERS/GEOMETRIES    | IN MILLIMETRES |
|--------------------------|----------------|
| Outer diameter (Dout)    | 188            |
| Inner diameter (Din)     | 110            |
| Height of the slot (hs)  | 20.5           |
| Width of the teeth (bts) | 4.8            |
| Stator back height (hrs) | 18.5           |
| Number of slots (Qs)     | 36             |
| Slot opening (bss1)      | 2.75           |

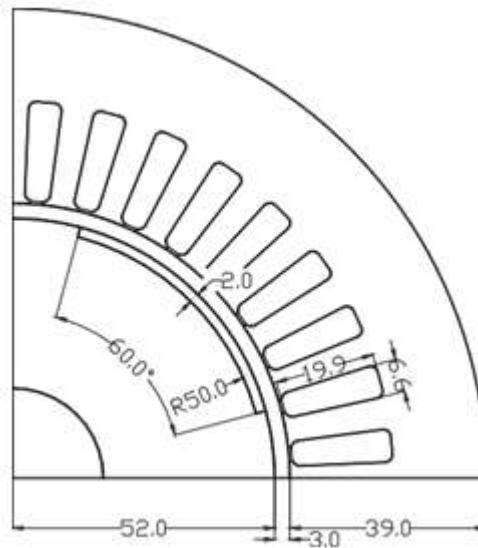


Fig. A1. Stator geometry.

### VIII. CONCLUSION

This study addressed the design of PMSMs for the traction of electric vehicles. The designs are based on an existing induction motor stator geometry. Performances of the prototype are expected to be superior over the induction motor. An IPM prototype motor has been built and more thoroughly measurements are still undertaking. These results will be further reported in a future study.

### ACKNOWLEDGMENT

Authors would like to thank Dr. D.A. Staton and Mr. E. Nordlund for their technical support in using Motor-CAD and FEMLAB.

**REFERENCES**

- [1] C. Mi, G.R. Slemon, R. Bonert, Modelling of iron losses of surface mounted permanent magnet synchronous motors, Proc. of IEEE IAS 36<sup>th</sup> annual meeting 2001, vol.4, pp2585-2591.
- [2] J.F. Gieras, M. Wing, Permanent Magnet Motor Technology, ISBN:0-8247-9794-9, Marcel Dekker, New York, 1997.
- [3] T. Sebastian, G.R. Slemon, "Operating limits of inverter driven permanent magnet motor drives", IEEE Trans. Ind. Appl. Vol. 23, No. 2, pp 327-333, Mar/April, 1987.
- [4] D.A. Staton, "Thermal computer aided design – advancing the revolution in compact motors", IEMDC'01, Boston, June, 2001.
- [5] S. Littmarck, Math, Models, Motion and More, PT Design Magazine, Penton Media, Cleveland, 2000
- [6] G.R. Slemon, "On the design of high-performance surface-mounted PM motors", IEEE Tran. Ind. Appl. Vol. 30, No. 1, Jan/Feb, 1994.
- [7] Y.K. Chin, E. Nordlund, D.A. Staton, Thermal Analysis – Lumped Circuit Model and Finite Element Analysis, International Power Engineering Conference (IPEC'03), Singapore, May, 2003, inpress.